Modal vibration modeling of a hemispherical turret in subsonic flow

Timothy J. Bukowski*[a], R. Mark Rennie[a], Matthew Kemnetz[c], and Stanislav Gordeyev[a]

[a]University of Notre Dame, Notre Dame, Indiana, 46556
[c]Air Force Institute of Technology, Wright-Patterson Air Force Base, Ohio 45433

ABSTRACT

Airborne beam propagation systems operate in high-jitter environments, where a significant contributor, known as aero-mechanical jitter, originates from unsteady aerodynamic forcing on the beam director. In this study, we investigate the aero-mechanical response of a hemispherical turret by simultaneously measuring optical jitter, surface pressure, and structural vibrations. A simplified turret geometry was designed to isolate key jitter mechanisms, and both experimental and numerical modal analysis were used to characterize the system vibration. Wind tunnel tests at subsonic Mach numbers were conducted with the turret mounted both inside and outside the tunnel to separate aerodynamic and structural contributions. To isolate key mechanisms, a simplified turret geometry with well-characterized material properties is employed. A reduced-order modal model is developed to connect surface pressure fluctuations to structural vibration and resulting beam jitter. This framework provides insight into the coupling between aerodynamic loading and optical stability, enabling more predictive jitter modeling for airborne optical systems.

Keywords: Jitter, Vibration, Modal Analysis, Hemispherical Turret, Aerodynamic Forcing

1. INTRODUCTION

There is considerable interest in airborne laser systems and much research has been done to make these feasible.[1–4] Hemispherical turrets are a popular beam director design due to their simple geometry and wide field of regard. However, protruding these blunt bodies from the aircraft into the flow creates significant aerodynamic disturbance and a strong unsteady wake. The diagram in Fig. 1 shows some of the main flow features.[5] This flow field has been studied in depth in wind tunnel tests,[6–10] flight tests,[6,11–13] and computational fluid dynamics (CFD)[14,15] and the fluid dynamics is fairly well understood.[16] The complicated wake behind the turret degrades a beam-propagation system's performance in two ways. First, it creates density fluctuations which lead to aberrations in the beam wavefront.[16] Second, the unsteady pressure field shakes the turret, which in turn shakes the optical components in the turret and leads to beam jitter. The jitter contributions from the air density fluctuations have been studied in depth[17,18]

However, the mechanical response of the optical train to the unsteady aerodynamic forcing is complex. Work has been done to show general relations between the pressure field and jitter. De Lucca et al. related beam jitter to the unsteady pressure field and showed the contribution of different features of the turret.[19–21] Mechanical jitter of the Airborne Laser Laboratory (ALL) was also studied.[22] Specific cases have had success in modeling and predicting system jitter levels. Griffin et. al. outlined the Line-of-Sight jitter modeling of the advanced tactical laser (ATL) system where the measured system closed-loop jitter was close to predictions.[23] Merritt outlined how local loop jitter can be estimated from system vibration measurements.[24] To investigate potential aeroelastic effects on the wake of a turret, Roeder and Gordeyev conducted experiments to examine the fluid-structure interaction of a turret in subsonic flow.[25] Their study showed that when the turret is allowed to oscillate due to unsteady flow forces, the resulting changes in the wake are minimal, even with relatively large oscillations (approximately 1 mm or 0.2% of the turret radius). Given that turret motion in practical applications is usually small, these findings imply that aeroelastic effects can be neglected when analyzing the wake dynamics and the associated unsteady forces on the turret.

*Further author information:
E-mail: tbukowski@nd.edu, Telephone: (574) 631-4280

Unconventional Imaging, Sensing, and Adaptive Optics 2025, edited by Jean Dolne, Santasri Bose-Pillai, Matthew Kalensky, Proc. of SPIE Vol. 13619, 136190Q · 2025 Published by SPIE
0277-786X · doi: 10.1117/12.3064058

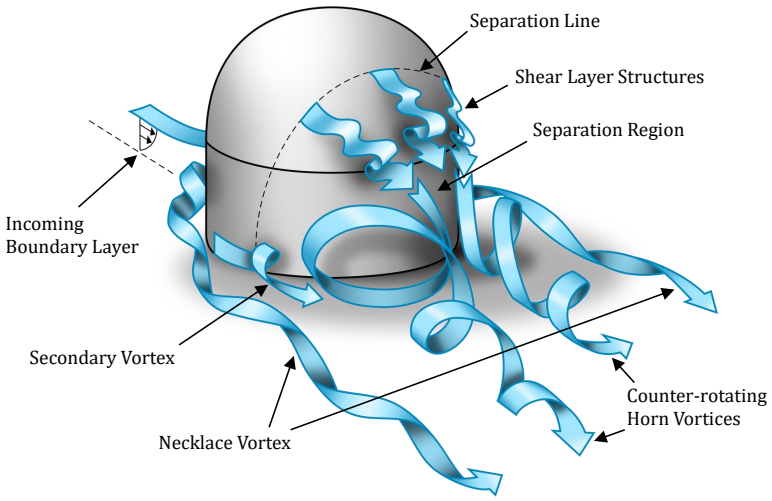

Figure 1. Sketch of main flow features in flow over a hemispherical turret. Figure reproduced from Kalensky et. al. 2024 with permission.[5]

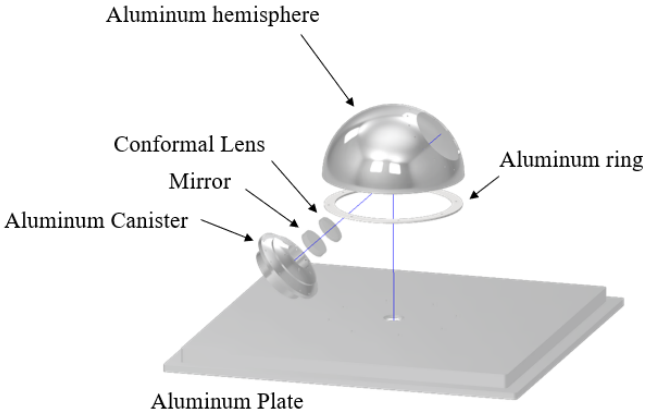

Figure 2. Exploded view of turret components and the plate that connects the turret to the wind tunnel.

The aeromechanical jitter resulting from this forcing is a difficult multidisciplinary problem that additionally involves the dynamic response of the mechanical structure, the behavior of the optical system, and the coupling between all these elements. Unfortunately, jitter analyses are typically performed for complicated optical configurations or prototype beam directors that are close to final, deployed systems. Even the AAOL turret used in the study described above had a coude path with around 20 distinct optical elements including windows, mirrors, lenses, and other components.[24,26,27] In the work presented here, we use a simplified turret design with significantly reduced degrees of freedom which should allow us to uncover and model relationships, mechanisms, and fundamental physics. An exploded view of the design is shown in Fig. 2. This design is discussed in more detail in Ref. 28.

In the following work we first introduce key concepts of vibration modal analysis in Section 2. Then in Section 3 we outline the experimental setup and how we determined our sensor placement. Next, in Section 4.1, the modal model is derived and tested using a calibrated hammer. We then perform wind tunnel tests and use the modal to analyze the forcing on the turret and compare with measured pressure in Sections 4.2 and 4.3.

2. VIBRATION MODAL ANALYSIS

Modal analysis in the context of structural response is a technique to mathematically model the dynamics of a system based on the idea that vibration is the sum of a series of independent vibration modes oscillating at

different natural frequencies. Numerical modal analysis typically is done through finite element analysis (FEA) where mass, stiffness, and damping matrices are created. Often times researchers will opt for experimental modal analysis where system identification is used to find modal shapes, natural frequencies, and damping coefficients, especially for complicated systems which may be difficult to model in FEA. Vibration modal analysis serves as the base for many integrated system models.[23,29] Modal analysis offers a simplified, reduced-order framework for examining how different forcing components contribute to vibration. This study employs both experimental and computational methods, with experimental system identification guiding refinements to the numerical model.

The books "Modal Analysis" by He and Fu[30] and "Modal Testing: Theory and Practice" by Ewins[31] are both well-known and contain a thorough overview of modal analysis. To briefly summarize modal analysis, the vibration of a system can be modeled with a 2nd order system of mass-spring-dampers

$$\mathbf{M}\ddot{\mathbf{x}} + \mathbf{C}\dot{\mathbf{x}} + \mathbf{K}\mathbf{x} = \mathbf{F} \tag{1}$$

where $\mathbf{M}$ is the mass matrix, $\mathbf{C}$ is the damping matrix, $\mathbf{K}$ is the stiffness matrix, $\mathbf{F}$ is a vector for the external forcing acting on the system, and $\mathbf{x}$ is a vector of the response (displacement) of each point in the system. This system of equations is strongly coupled and difficult to solve. However, a coordinate transformation to modal coordinates can be performed

$$\mathbf{x} = \mathbf{\Psi}\mathbf{q} \tag{2}$$

where $\mathbf{\Psi}$ is a matrix of the mass-normalized mode shapes and $\mathbf{q}$ is a vector of the modal temporal coefficients. The mode shapes are found by solving the eigenvalue problem of the undamped homogeneous system and are mass orthogonal. This transformation involves projecting the mass, damping, and stiffness matrices, as well as the force vector on the mode shapes. This projection diagonalizes the modal mass and stiffness. Under the assumption of modal viscous damping, the equation for a given mode, i, becomes

$$\ddot{q}_i + 2\zeta_i\omega_{n,i}\dot{q}_i + \omega_{n,i}^2 q_i = f_i \tag{3}$$

where ζ is the modal damping coefficient and ω_n is the mode's natural frequency. Here the modal force is defined by mapping the force vector onto the mode as $f_i = \Psi_i^T F$. With this change to modal coordinates, there is now an uncoupled system of single input single output systems where each of the vibration modes can be treated as its own vibration system.

When using experimental modal analysis, system identification must be used to compute the modal parameters from measured data. There are a wide range of methods for computing these variables. Dossing created a tutorial on experimental modal analysis.[32,33] Omar gives some of the simpler methods for retrieving modal parameters as follows.[34] To obtain modal frequencies, one can instrument the structure with accelerometers and perform a hammer test or sine-sweep, then find the peaks in the signal in the frequency domain. To find the modal shape one can look at the correlation and relative phase between sensors at different points. The damping ratio can be estimated from the full-width half maximum (FWHM) of the spectral peak[35] or simply fitting the SDOF transfer function to the spectra.[36] However, for experimental data, the spectra are generally noisy and the FWHM is unclear, so Kim et. al introduced a similar method that fits the cumulative spectrum to find the damping.[37] Many commercial applications and code libraries exist for system identification.[38–40]

Many times it is useful to relate the forcing to the vibration response through a transfer function. In modal displacement coordinates this transfer function is referred to as modal receptance. The receptance is defined as

$$H_i(\omega) = \frac{\mathcal{F}\{q_i\}}{\mathcal{F}\{f_i\}} = \frac{1}{k_i - \omega^2 m_i + i\omega c_i} \tag{4}$$

where k_i is the modal stiffness, c_i is the modal damping and $k_i = \omega_{n,i}^2 m_i$ and $c_i = 2\zeta_i\omega_{n,i}m_i$.

We can relate the receptance to the frequency response function (FRF), which is the transfer function between displacement at a given spatial location to the force applied at a different location, as

$$R_{jk}(\omega) = \frac{\mathcal{F}\{x_k\}}{\mathcal{F}\{F_j\}} = \sum_i \Psi_{i,j}\Psi_{i,k}H_i(\omega) \tag{5}$$

where R is a symmetric matrix, $R_{jk} = R_{kj}$, j denotes the location where the force is applied, and k denotes the location where the displacement is measured.

For the case of the turret being studied in this work, mirror tilt, θ can also be estimated from the modal model as

$$\theta = \sum_i \theta_{\Psi_i} q_i \tag{6}$$

where θ_{Ψ_i} is the tilt across the mirror in the mode shape Ψ_i.

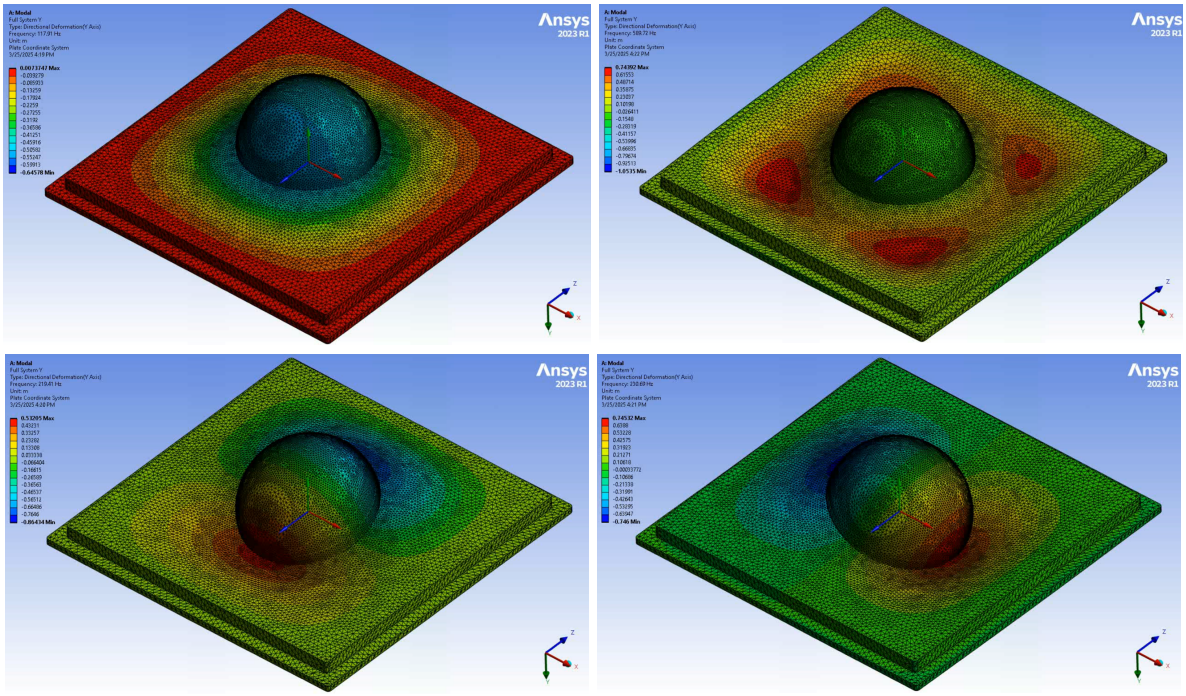

Figure 3. Vibration modes of the plate and turret assembly up to 650 Hz.

For this research, we chose to use finite element analysis in Ansys Mechanical to determine resonant frequencies and mode shapes for the turret and base plate. These results were shown in detail and compared to experimental measurements in Ref. 28. Here a summary of the FEA analysis is discussed. The four modes with the lowest natural frequencies are shown in Fig. 3. In the modal analysis, the focus was on identifying low-frequency modes of around 200 Hz or lower, that could be excited by the flow and result in significant tip/tilt of the optical canister mounted in the turret. Figure 3 shows that the lowest-frequency vibration modes of the turret actually originate entirely from deformation of the base plate onto which the turret is mounted, rather than from deformation of the turret itself. The experimental model still represents a realistic aeromechanical jitter problem, however, since the primary source of vibration of the system is expected to be aerodynamic forcing from the flow around the turret.

The frequencies of the modes are included in Fig. 3, and are 118 Hz for the drumming mode in the top left subplot, 219 Hz and 231 Hz for the two rocking modes at the bottom of the figure, and 650 Hz for the top right mode shape. The spectral content of the aerodynamic forcing is expected to be below a Strouhal number of 0.5[25] where Strouhal number is the non-dimenionalized frequency $St_D = fD/U_\infty$ which accounts for turret diameter, D, and freestream velocity, U_∞. For Mach numbers from 0.3 to 0.5 in the wind tunnel, $St_D = 0.5$ corresponds to frequencies of around 200 - 350 Hz. There is a strong peak in the spectra from vortex shedding around $St_D = 0.2$, which corresponds to frequencies around 80 - 160 Hz.[25]

The FEA analysis also allows for visualization of the mode shapes to identify and quantify of the sources of the motion of the optical canister and hence the beam jitter. The materials and design of the model parts were adjusted until vibration modes in the desired frequency range were achieved. The vibration modes are explained in our previous work in Ref. 28. Since that preliminary work, two improvements to the FEA model were implemented that significantly improved the match between the FEA mode frequencies and the experimentally measured ones. The first was changing the method for modeling the connection of the turret to the plate in the FEA model. Previously, these two parts were bonded along the entire contact surface between the bottom of the turret and the mounting plate, but this produced too stiff a connection which led to computed modal frequencies that were too high. To improve the FEA simulation, we switched the bonded connection between the turret and mounting plate to only the locations of the bolts in the real turret; this adjustment provided a more flexible interface, lowered the frequencies, and led to excellent match of modal frequencies between the FEA and experimental model within 1 Hz for the case of a free boundary condition on the edges of the plate. This suggests the model accurately captures the structural properties of the turret and plate. However, when the turret and plate are mounted into the wind tunnel, there is no longer a free boundary condition; further, bolts securing the turret base plate to the tunnel walls do not produce a perfectly stiff connection. Originally, the connection of the plate to the tunnel was modeled as a perfectly stiff, zero-displacement boundary condition, however, it was found that the modal frequencies were too high. It was discovered that using an elastic boundary condition on the edges of the plate with a stiffness of 6.256 x 10^{10} N/m^3 led to much better agreement with the frequencies found empirically. These changes did not change the mode shapes by any noticeable amount.

3. EXPERIMENTAL SETUP

Wind tunnel testing was performed at the University of Notre Dame's White Field Mach 0.6 wind tunnel. This wind tunnel has a 3 $\times$ 3 ft test section and data were collected at a freestream Mach numbers of 0.08 - 0.5 ($Re_D \approx 0.3 - 2 \times 10^6, U_\infty \approx 46 - 395$ mph). This facility is particularly useful as the dynamic pressures are similar to those observed in flight.

Shack–Hartmann wavefront sensor (SHWFS) measurements were taken to obtain global and local tilts on the beam, using the optical layout shown in Fig. 4. A 532 nm Novanta opus continuous laser source was used which was expanded to a 25 mm aperture then expanded again through an f400 and f800 lens to a 50 mm aperture beam that was reflected off the turret canister mirror and passed back through the telescope reducing it back to a one-inch beam. The mirror was then reimaged onto the SHWFS by a f285 and f250 lens, contracting the beam to 22.3 mm aperture. SHWFS images were taken using a Phantom v2512 high-speed camera. The beam was also focused through a f300 lens onto a position sensing device (PSD) to provide an additional measurement of global tilt.

Thirteen accelerometers were placed around the turret and plate in positions shown in Fig. 9 to provide vibration measurements. Accelerometers 1-12 were single-axis PCB 352C33 sensors and accelerometer 13 was a tri-axis PCB 356A14. Accelerometers 1-8 were read through a PCB 483C05 signal conditioner while 9-13 were read by PCB 482A22 signal conditioners. Seven accelerometers were placed around the plate. The three-axis accelerometer was placed on the top of the turret to capture turret motion. Three accelerometers were placed on the canister for redundant measurement of tilt. One sensor was placed on the test section wall downstream of the turret and plate. The last sensor was placed on the optics table. All accelerometer and PSD data were collected using an NI-9222 data acquisition module. Pressure measurements were taken using 10 Kulite XT-140-10D and 10 Kulite XT-140-15D pressure transducers, which were read through a NI PXIe-4331 signal conditioning module on a NI PXIe-9078 data acquisition system. The locations of these sensors is shown in Fig. 7. All data was collected at a sampling rate of 10 kHz and all sensors were triggered together. Accelerometer, PSD, and Kulite data were recorded for 30 seconds, while SHWFS data were recorded for about 4 seconds. Flow speed measurements were obtained using the dynamic pressure measured with a Pitot probe and a Setra 270 transducer at the entrance to the test section.

Impact response tests of the turret model were also carried out using a PCB 086C03 calibrated hammer which was read through a PCB 482A22 signal conditioner using the NI-9222 module. The optical canister mounted in the turret had an elevation angle of 43 degrees relative to the floor of the tunnel and an azimuthal angle of

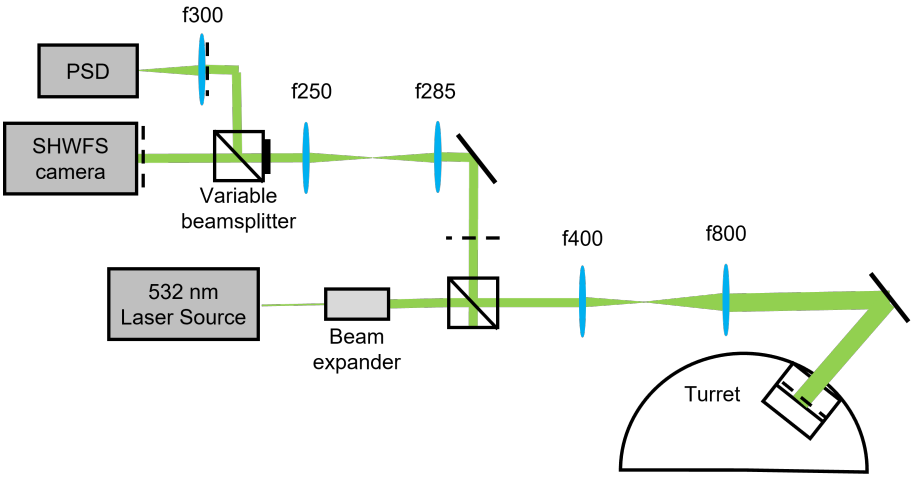

Figure 4. Diagram of optical beam train.

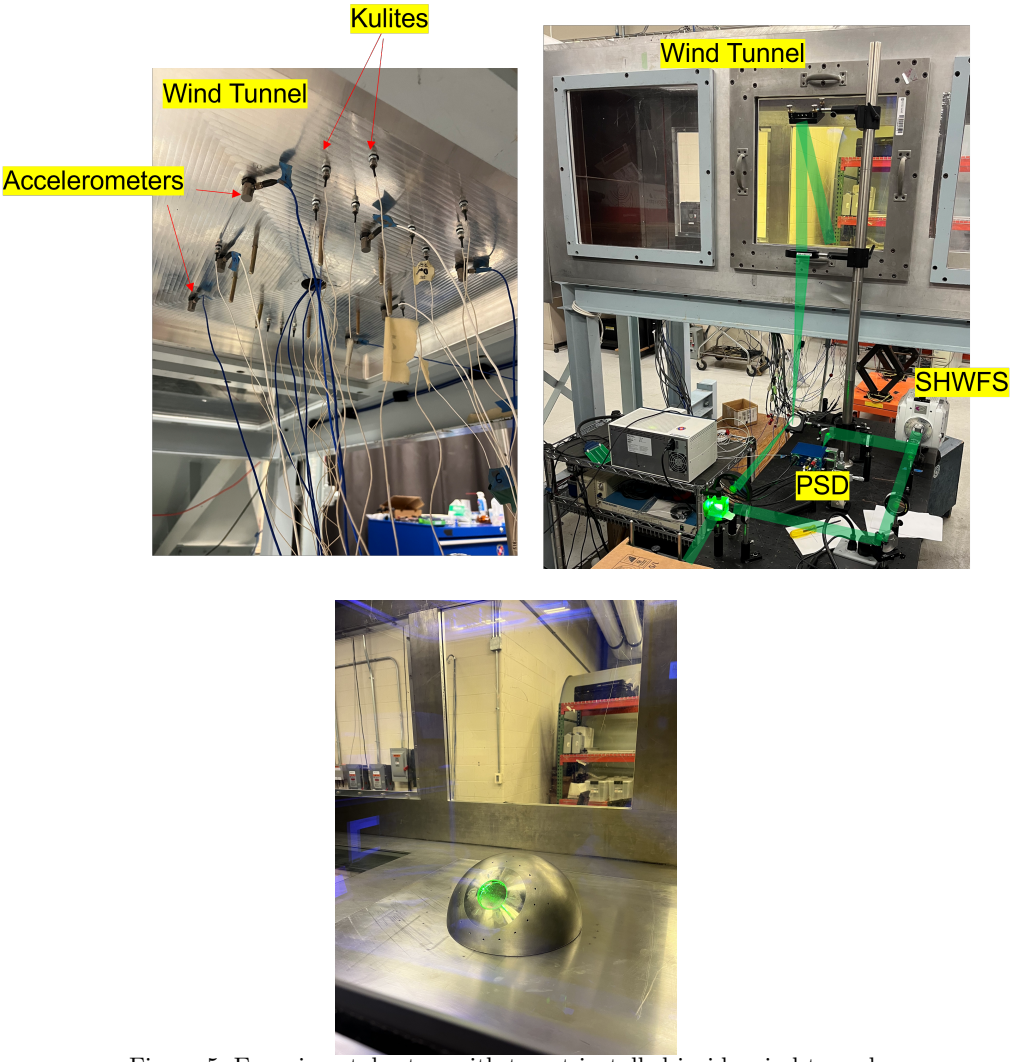

Figure 5. Experimental setup with turret installed inside wind tunnel.

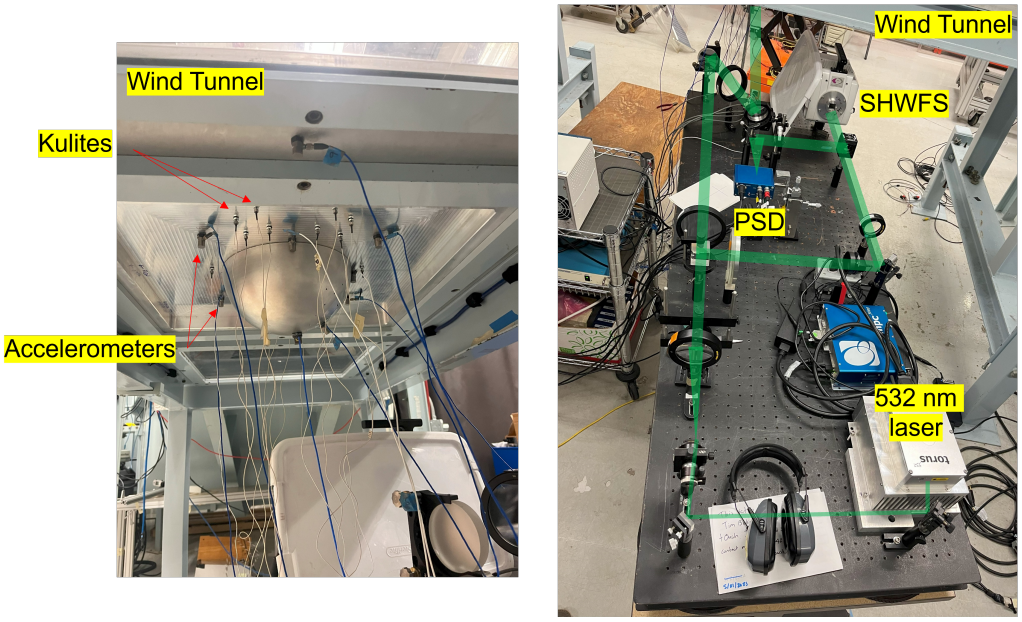

Figure 6. Experimental setup with turret installed outside of the wind tunnel.

90 degrees relative to the flow direction. The 43 degree elevation angle was chosen to maximize useable optical access to the canister mirror from the optical table outside the test section. The setup is shown in Fig. 5.

When the turret is in the wind tunnel, it is excited by both the flow and the base motion of the tunnel walls. As such, we also tested a second configuration in which the turret was mounted to the outside of the tunnel with the wind tunnel running, in order to capture the influence of just the tunnel-related base vibration on the turret jitter. By mounting the turret underneath the tunnel, we can retain very similar vibration modes and bounce a beam off the canister to measure tip tilt, while eliminating aerodynamic effects on the turret. The test setup with the turret mounted outside the tunnel is shown in Fig. 6.

3.1 Sensor placement

We are interested in measuring modal forcing and response in order to test and use our modal model. However, to calculate the modal coefficient of the vibration, the displacement field of the entire turret is needed, and to calculate the aerodynamic forcing, the pressure over the wetted surface is needed. However, we had a limited number of sensors, so a study was performed looking into the optimal location for the accelerometers and pressure sensors, as well as the best way to calculate the modal response and forcing coefficients from the sensor data. The methods used for this optimization are discussed in detail in Ref. 41, where we looked into how well we could reconstruct the surface pressure field using a sparse set of pressure sensors. This study showed that over 100 pressure sensors would be needed to reconstruct the turret pressure field with reasonable accuracy of an L2 norm error of about 15% of the pressure rms. Instead, here we directly mapped from the pressure sensor data to the modal forcing coefficients using Linear Stochastic Estimation (LSE)[41,42] as

$$\hat{\mathbf{f}} = \mathbf{L}\mathbf{y}, \text{where } \mathbf{L} = \mathbf{f}\mathbf{y}^T(\mathbf{y}\mathbf{y}^T)^{-1} \tag{7}$$

where $\mathbf{f}$ is the vector of the modal forcing coefficients due to the pressure field on the turret, $\mathbf{L}$ is the estimation coefficient matrix, and $\mathbf{y}$ is a vector of the pressure sensor measurements. The $\mathbf{L}$ matrix was trained using pressure sensitive paint (PSP) data from the experiment done in Ref. 25, where the true modal forcing coefficients were found by converting the full surface pressure field data to a force on each mesh element, $\mathbf{F}$, which were then projected onto the vibration modes as $f_i = \Psi_i \mathbf{F}$. Pressure values at the pressure sensor locations were then selected from the PSP data and the $\mathbf{L}$ matrix was calculated. The resulting reconstructed forcing coefficient error is shown as a function of the number of sensors for the first three vibration modes in Fig. 8. These plots also

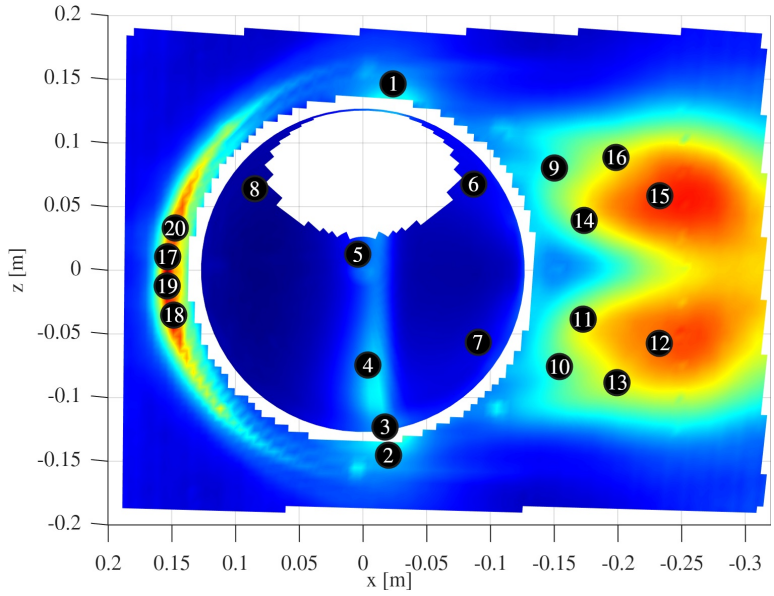

Figure 7. Pressure sensor placement overlayed on pressure rms field for M=0.5 case

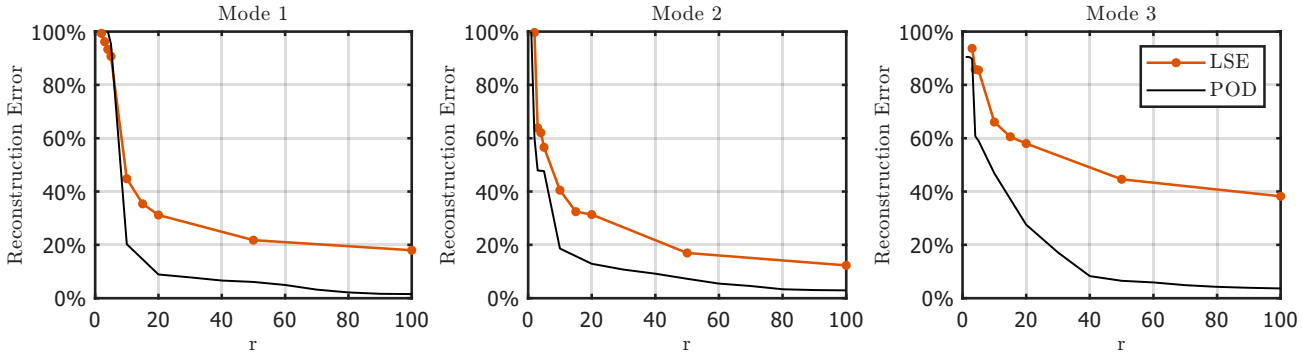

Figure 8. Reconstruction error of modal response coefficients estimated from sparse set of accelerometer measurements. Error reported as a percent of the rms of the true forcing coefficient.

show the reconstruction error if the forcing coefficients are estimated using an increasing number of POD modes. POD optimally reduces the order of data by energy and this curve serves as a lower limit on the coefficient error for a given number of sensors. We can see there is a knee in the error curve around 20-30 sensors, after which adding more sensors does not significantly improve performance. We had 20 sensors on hand which we believed to be sufficient.

The pressure sensor placement used to create the results in Fig. 8 was not fully optimized, so further placement optimization was performed to improve accuracy. Several optimization methods were tried as well as random placement; however, we found that handpicked placement led to the best performance with error around 20-40% depending on the mode. Here, the sensors were placed close to regions of large rms pressure variations and were placed closer together in regions with short spatial correlation lengths in the flow. The pressure sensor layout is shown in Fig. 7 and is overlaid on rms pressure field. These errors are relatively high, but provide a starting point. Further, note that the reconstruction used here only accounts for spatial information. Algorithms such as SHRED[43] that include temporal information allow for much higher accuracy reconstruction using far fewer sensors and could be added in the future for better fidelity.

Table 1. Kulite Pressure Sensor Locations with Coordinates

Sensor	S/N	Model	x [cm]	y [cm]	z [cm]
1	50	Kulite XT-140-10D	-2.35	0.00	14.60
2	64	Kulite XT-140-10D	-1.98	0.00	-14.50
3	651	Kulite XT-140-15D	-1.73	2.64	-12.30
4	652	Kulite XT-140-15D	-0.39	10.30	-7.45
5	653	Kulite XT-140-15D	0.41	12.60	1.26
6	654	Kulite XT-140-15D	-8.67	6.35	6.77
7	656	Kulite XT-140-15D	-9.03	6.92	-5.64
8	657	Kulite XT-140-15D	8.51	6.92	6.41
9	48	Kulite XT-140-10D	-15.00	0.00	8.00
10	4-62	Kulite XT-140-10D	-15.40	0.00	-7.56
11	4-68	Kulite XT-140-10D	-17.25	0.00	-3.84
12	4-69	Kulite XT-140-10D	-23.25	0.00	-5.74
13	4-70	Kulite XT-140-10D	-19.90	0.00	-8.80
14	4-74	Kulite XT-140-10D	-17.25	0.00	3.84
15	504	Kulite XT-140-10D	-23.25	0.00	5.74
16	518	Kulite XT-140-10D	-19.90	0.00	8.80
17	658	Kulite XT-140-15D	15.37	0.00	1.23
18	659	Kulite XT-140-15D	14.90	0.00	-3.52
19	660	Kulite XT-140-15D	15.37	0.00	-1.23
20	661	Kulite XT-140-15D	14.90	0.00	3.52

The accelerometers on the plate were used to estimate the vibration modal response coefficient, q. The measured acceleration was converted to displacement by dividing the acceleration by the ω^2 in the frequency domain. The QR factorization based sensor placement[41,44,45] using the vibration mode shapes was found to work quite well for the accelerometers. The method essentially places sensors at the peaks in the vibration mode shapes. The resulting sensor placement is shown in Fig. 9 where it is overlaid on vibration mode 4. In addition to LSE, simply projecting the measured displacements onto the vibration mode shapes as $\hat{\mathbf{q}} = \mathbf{\Psi}^{\mathbf{T}}\mathbf{x}$ was tested. For both methods, it was found that errors less than 10% in the modal response coefficient were achievable by using only 7 accelerometers. The error in the coefficient calculation is shown as a function of the number of sensors in Fig. 10. The modal projection method was chosen due to its simplicity as LSE requires training, while the modal projection does not.

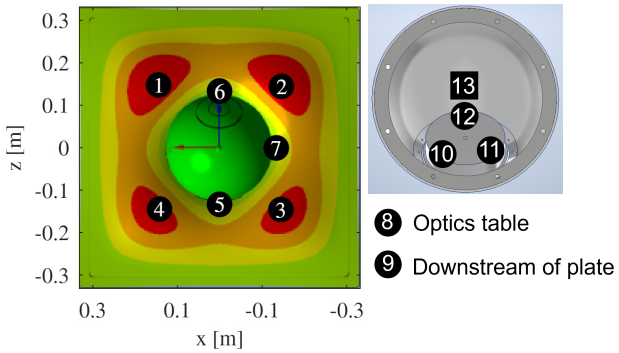

Figure 9. Accelerometer locations overlayed on vibration mode

Table 2. Accelerometer Locations with Coordinates

Sensor	S/N	Model	x [cm]	y [cm]	z [cm]
1	LW160332	PCB 323C33	14.44	-0.63	14.76
2	LW160334	PCB 323C33	-14.60	-0.64	14.45
3	LW160335	PCB 323C33	-14.45	-0.64	-14.61
4	LW160336	PCB 323C33	14.29	-0.64	-14.45
5	LW160674	PCB 323C33	0	-0.64	-13.34
6	LW160675	PCB 323C33	0	-0.64	13.34
7	LW160676	PCB 323C33	-13.34	-0.64	0
8	LW160677	PCB 323C33	on	optics	table
9	LW160679	PCB 323C33	-38.1	-3.81	0
10	LW160680	PCB 323C33	-3.23	-10.85	10.06
11	LW138670	PCB 323C33	3.23	-10.85	10.06
12	LW138672	PCB 323C33	0	-14.73	6.35
13x	127112	PCB 356A14	0	-13.34	0
13y	127112	PCB 356A14	0	-13.34	0
13z	127112	PCB 356A14	0	-13.34	0

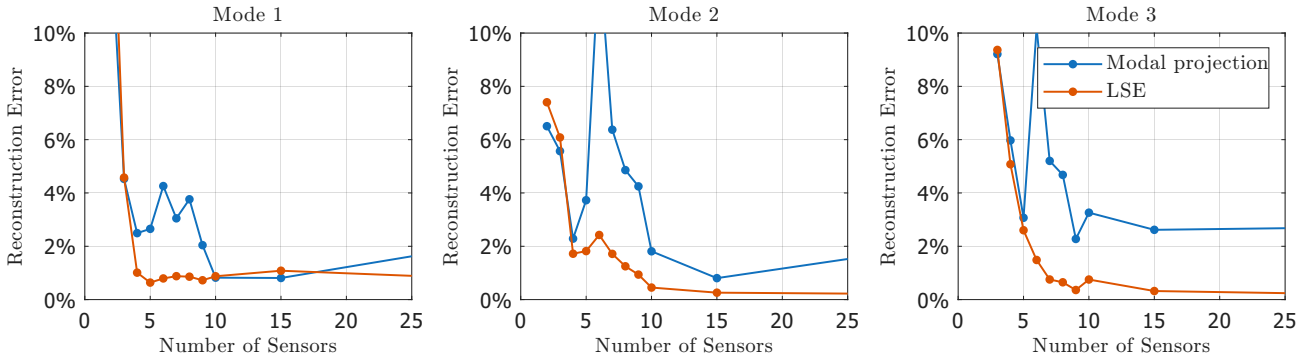

Figure 10. Reconstruction error of modal forcing coefficient from sparse set of pressure measurements.

4. RESULTS

Results from three scenarios are presented in the following section. First, calibrated hammer testing was performed where both forcing and response could be measured which allowed us to test the performance of the modal model. Next the turret was placed outside of the tunnel to measure vibration due to the empty tunnel motion and finally the turret was placed inside the tunnel where it was subjected to forcing from both the tunnel and aerodynamic forcing.

4.1 Hammer test

We first performed calibrated hammer testing. This was done for a series of different scenarios to test both our modal model and the finite element (FEA) predictions of the vibration modes. The first test was a free boundary condition case which was approximated experimentally by setting the plate on two tire inner tubes. This test produced very good agreement between the measured mode shapes and frequencies those predicted by the FEA. The condition with the turret outside the tunnel was tested, and then with the turret inside the tunnel. In this section, only the hammer test of the turret inside the tunnel is discussed. The alignment of the mode shapes and modal frequencies was discussed in our previous work in Ref. 28.

The receptance was found using the estimated $\hat{\mathbf{q}}$ and $\hat{\mathbf{f}}$ following eq. 4 and is shown in Fig. 11 as the black line for the first 3 modes. The theoretical receptance based on the modal parameters (eq. 4) is shown by the dashed red line. In this case the hammer was tapped at the location of accelerometer 3 (see Fig. 9). The damping coefficient needed to define the theoretical receptance was found by using the cumulative spectrum method described in Ref. 37; however, in some cases, the damping ratio was adjusted to better fit the spectrum

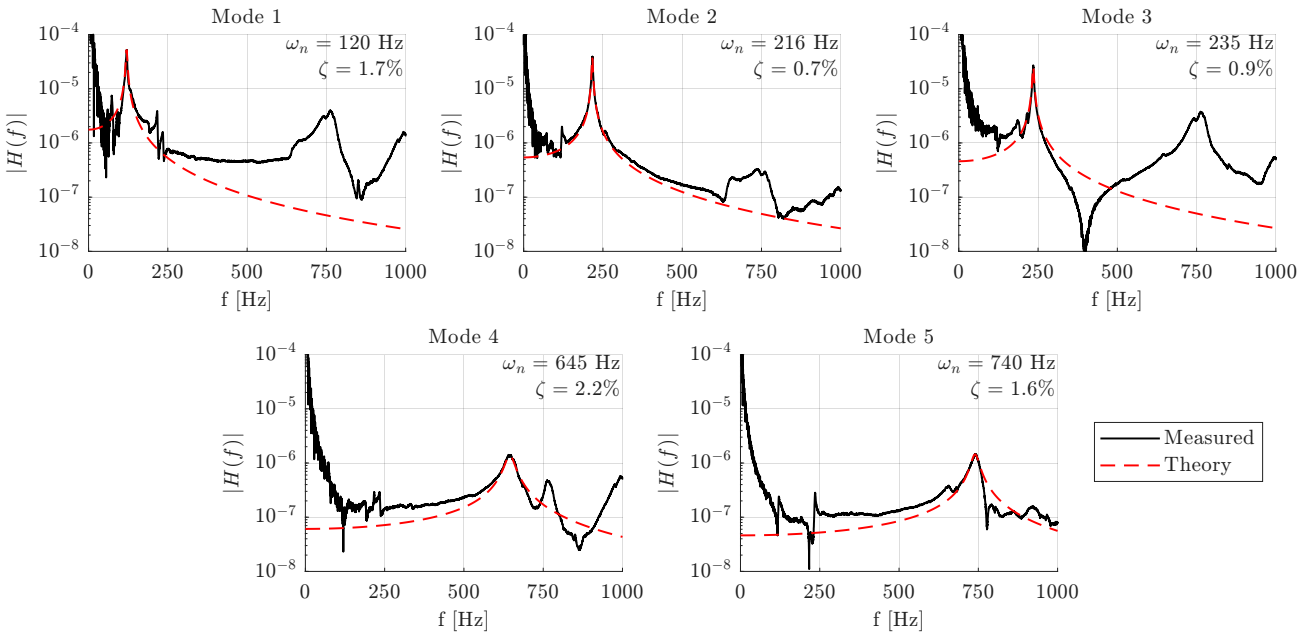

Figure 11. Measured receptance compared to theoretical fit for calibrated hammer test.

peak. The modes had fairly low damping with modes 1 - 3 being around 1%, while 4 - 5 are around 3%. Figure 11 shows that the measured and theoretical receptance curves agree very well, within about ±25 Hz of the natural frequency of the mode, which makes sense as the theoretical curve parameters are adjusted to fit in this region. However, outside of this region the two curves quickly diverge, with the measured receptance being multiple orders of magnitude higher or lower than the theoretical receptance at some frequencies. This is due to the fact that there are multiple peaks in the measured receptances, which is likely a result of the modal coefficient reconstruction. While the reconstruction does a good job of separating the first three modes, as evidenced by the strong single peak in the lower frequency range, there is also a peak at around 765 Hz which corresponds to the fifth mode. This suggests that this mode is coupled with the lower frequency modes, however, if this were the case then the lower frequency peaks should also appear in the receptance for mode 5 which they do not. Additionally, preliminary testing indicates that, for example, tapping the hammer at the location of accelerometer 6 does in fact excite mode 5, despite accelerometer 6 being at a node where it should not directly excite mode 5. Further study is required into the best method of calculating the modal response coefficient.

The modal receptances were converted to a series of FRFs following eq. 5 and were compared to the measured FRF directly relating measured displacement and forcing. In this case the theoretical modal models were scaled through the mode shapes to get the full field, instead of mapping the experimental data onto the mode shapes. The measured FRFs between a hammer strike applied at accelerometer 3 and the measured displacement at sensors 1, 5, and in the y-component of 13 are shown in Fig. 12. We can see that in this case the measured and theoretical FRFs match very well along the entire frequency range of interest between 100 Hz and 1000 Hz for sensors 1 and 5 which are on the plate. The FRF for sensor 13y on the turret has some disagreement for the higher frequency modes. Below 100 Hz the measured FRFs severely overestimate due to the integration of noise from the measured acceleration.

We are ultimately interested in the jitter on a beam that would be projected from the turret. The y-component beam jitter spectrum measured on a beam reflected from the optical canister mounted to the turret is shown in Fig. 13. The local jitter measured by the SHWFS was spatially averaged across each frame to give a global jitter timeseries. The spectrum of this timeseries is shown as the black curve. The jitter measured using the position sensing device is shown as a yellow curve and has excellent agreement with the SHWFS up to about 1000 Hz where the PSD begins to overestimate jitter. Jitter was also estimated from the modal model and is shown as a red curve. Here the modal response coefficients were estimated from the accelerometer measurements, and then

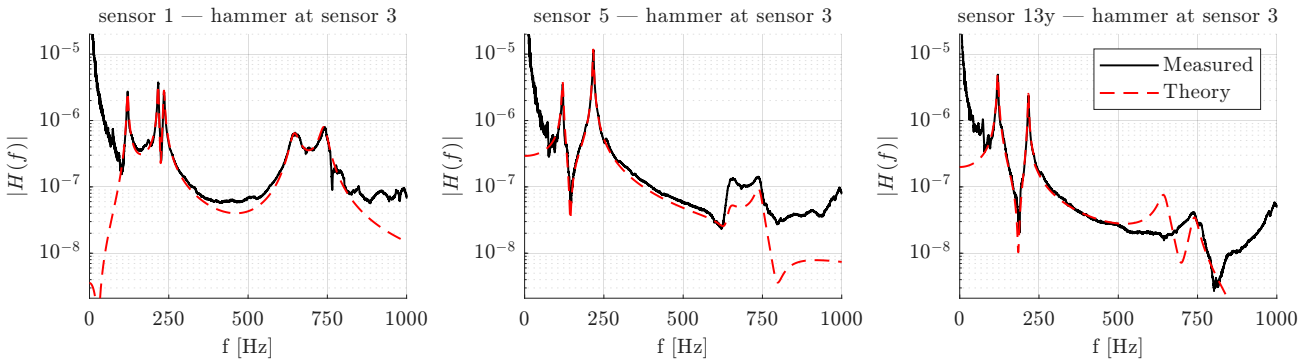

Figure 12. FRF at accelerometer 1, 5, and 13y for a hammer hit at accelerometer 3.

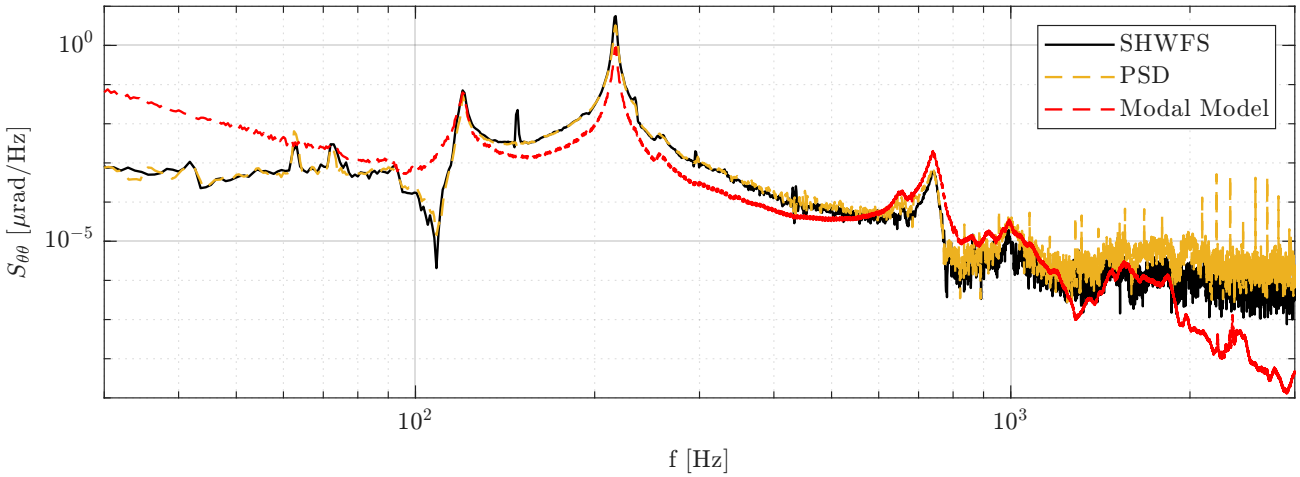

Figure 13. Jitter spectra for hammer test.

each modal coefficient was multiplied by the tilt on the mirror in each respective mode's shapes to give a modal contribution and these were summed to give the total tilt. Overall the shape of the jitter spectrum from the modal model matches the actually measured jitter. However, below about 70 Hz the modal model jitter is much larger due to integration of measurement noise when integrating the measured acceleration to get displacement. This also leads to an underestimate of jitter above 1 kHz. The peak of the 120 Hz mode matches quite well between the model and the measurement, however, there is an anti-node that the model misses at around 110 Hz. The model also underestimates the 216 Hz mode peak and as a result slightly underestimates the spectrum from 100 - 700 Hz. We can integrate over the 100-1000 Hz range, which is where we can expect agreement between the accelerometer based modal model jitter and the measured jitter, to give a band-integrated rms

$$\sigma_{\theta,\mathrm{BI}} = \sqrt{\int_{0.1\ \mathrm{kHz}}^{1\ \mathrm{kHz}} S_{\theta\theta}(f)df} \tag{8}$$

The BIRMS was 6.7 μrad for the SHWFS, 5.5 μrad for the PSD, and 3.0 μrad for the model-estimated jitter.

The modal model was also used to study the different forcing inputs. From the estimated modal response coefficients, we can either go through the time domain and follow equation 3 or we can perform the analysis in the frequency domain and simply divide the measured response spectra by the receptance functions shown in Fig 11. The calculated forcing coefficient is plotted in Fig. 14 for the first three modes in red. The forcing coefficient spectra derived from the calibrated hammer data are shown in black. For mode 1 the estimated forcing spectrum significantly overestimates the actual forcing by multiple orders of magnitude at the higher frequencies. This mismatch arises because of the difference between the measured and theoretical receptances shown in Fig.

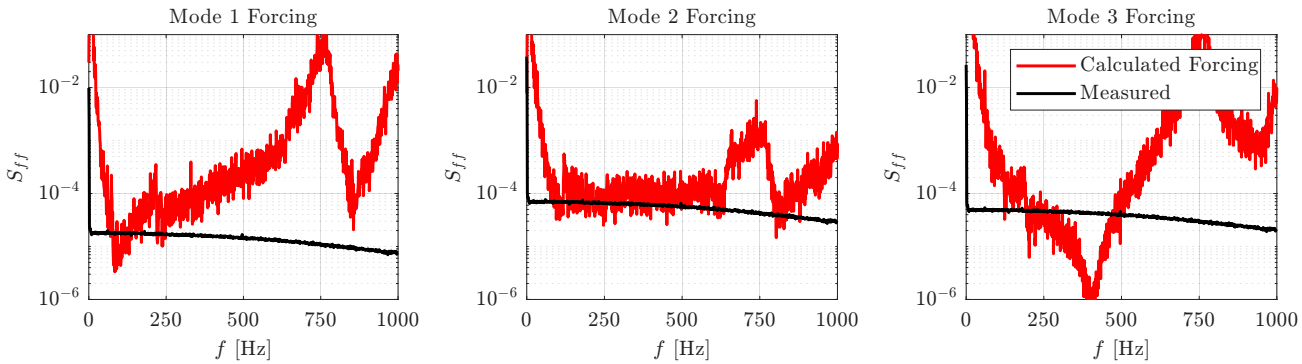

Figure 14. Modal forcing spectrum computed from accelerometer measurements compared to that computed from calibrated hammer.

11; however, there is good agreement between the measured and calculated forcing spectra around the natural frequency ±25 Hz, where the measured and theoretical receptances in Fig.11 match more closely. A similar trend exists for mode 3 where the estimated forcing is only close to the actual forcing around the natural frequency. For mode 2, however, the measured receptance matches the theoretical receptance over a larger range and so the estimated modal forcing spectra also matches the actual forcing over a larger range of frequencies, from about 100 - 625 Hz. While this shows that this methodology for backing out forcing is accurate only over a small range of frequencies around a given mode's natural frequency, it is clear that in order to accurately estimate forcing over a larger range, better agreement is needed between measured and theoretical receptance.

4.2 Tunnel only forcing

With this understanding of the of the limits and capabilities of the model, we next applied the model to wind tunnel data. We first looked at the case with the turret mounted to the outside of the tunnel where it is only exposed to forcing from the wind tunnel vibration, with no aerodynamic forcing.

The modal response coefficient spectra of the first 5 modes are shown in Fig. 15, for a test-section Mach number of M = 0.3. The response spectra look similar to the receptance spectra derived from the hammer test in Fig. 11 with the first three modes having fairly clearly defined peaks at their natural frequencies, but also include significant peaks at the 765 Hz mode. On the other hand, the 650 Hz and 765 Hz modes have only clear peaks at their natural frequencies. In all of the responses we see clear narrow peaks at the wind tunnel fan blade-pass frequency, which is marked by a dashed black line, and its harmonics.

The modal forcing was computed using the receptance spectra determined in the hammer tests. This was done using both the theoretical receptance and the measured receptance. The resulting forcing spectra are shown in Fig. 16 where the forcing computed using the theoretical receptance is the orange curve while the brown curve is the experimentally measured receptance. These curves overlap around each mode's natural frequency which is where the theoretical and measured receptances match. In other words, the estimated force is more reliable where these two curves overlap. The theoretical modal forcing spectrum was integrated over the range of trustworthy frequencies around the natural frequency to give a band-integrated rms

$$\sigma_{f,\mathrm{BI}} = \sqrt{\int_{\omega_n - 25\ \mathrm{Hz}}^{\omega_n + 25\ \mathrm{Hz}} S_{ff}(f) df} \tag{9}$$

which is shown as a function of Mach number in Fig. 17 for modes 1-5. As expected, the forcing increases with Mach number. Modes 4 and 5 have the lowest amplitude forcing, followed by mode 2, then mode 1. Mode 3 has the highest forcing.

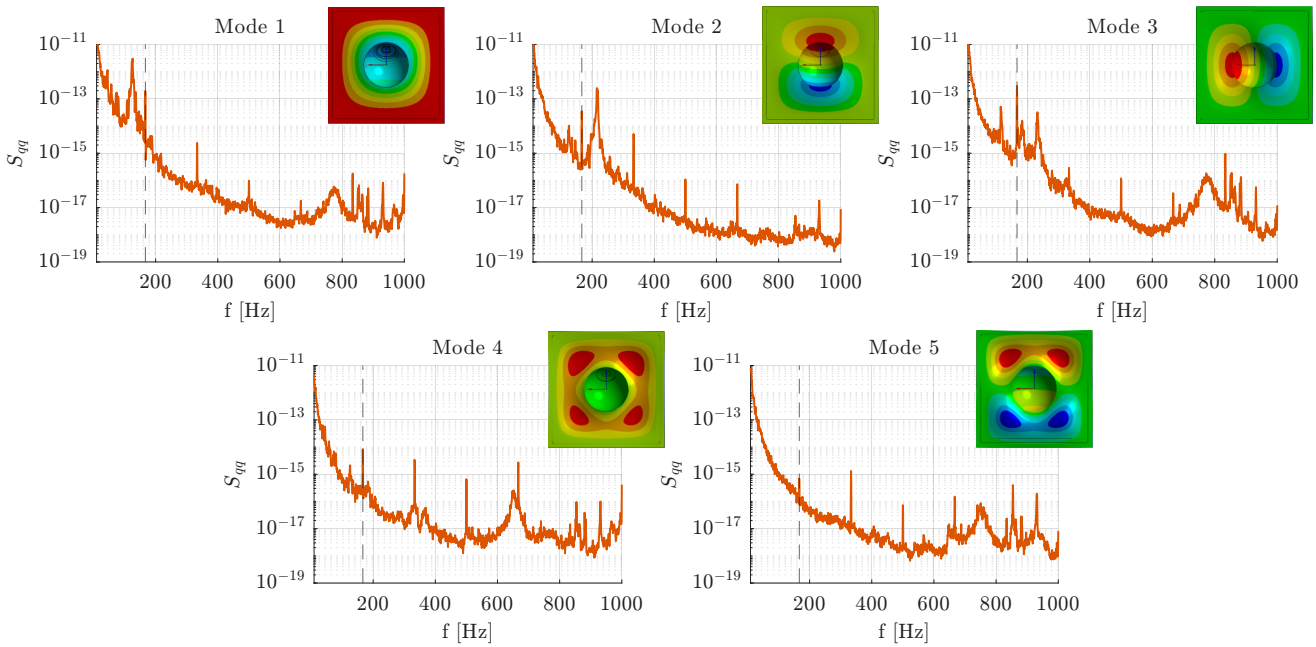

Figure 15. Modal spectra with mode shape insets. The wind tunnel fan blade-pass frequency is marked by a vertical dashed line.

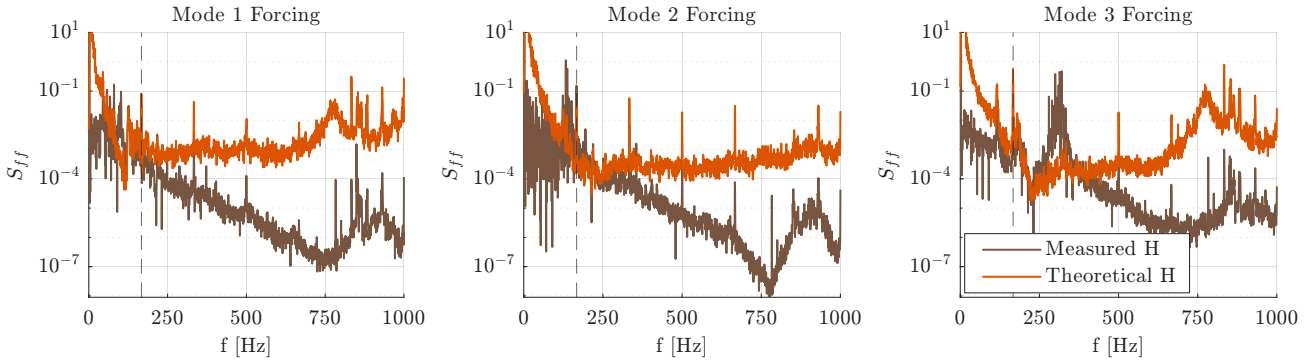

Figure 16. Modal forcing spectra computed using measured receptance and theoretical receptance.

The jitter spectrum for the M = 0.3 run is plotted in Fig. 18 for both the SHWFS and the modal model. Again the model overestimates jitter for the low frequencies under 100 Hz and underestimates for the larger frequencies over 1000 Hz. The 120 Hz mode matches quite well, while the 216 Hz mode is slightly low for the model. In this case there was additional energy from 50-100 Hz in the SHWFS jitter that did not appear in the model jitter spectrum. This is likely due to vibration of the optics table, as this frequency band was also excited for the accelerometer attached to the table. We believe one of the tire innertubes that are place under the optics table to reduce vibration was flat, which led to additional vibration of the table.

The BIRMS, $\sigma_{\theta,BI}$ of jitter was computed for the SHWFS and modal model jitter as a function of the Mach number, which is plotted in Fig. 19. As the Mach number increases the model reconstructed jitter underestimates the SHWFS.

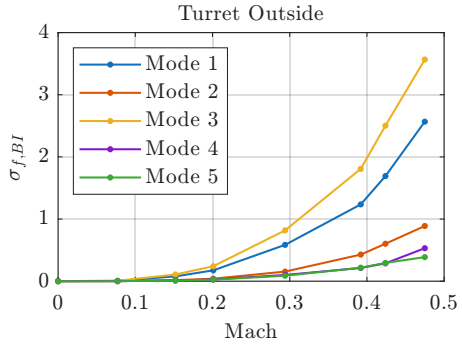

Figure 17. BIRMS modal forcing as a function of Mach number.

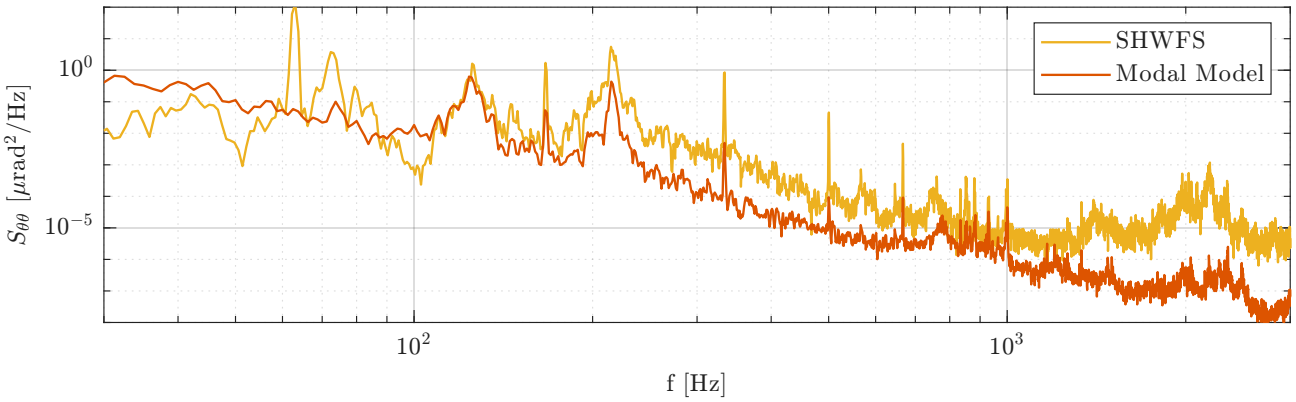

Figure 18. Jitter spectra for case where turret is mounted outside of wind tunnel.

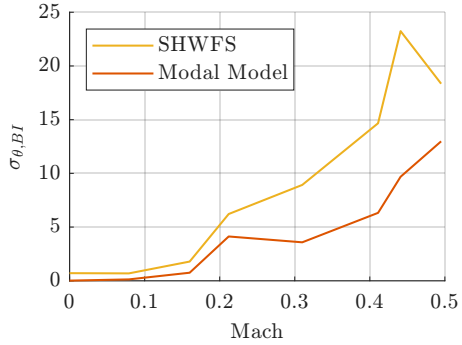

Figure 19. BIRMS jitter as a function of Mach number.

4.3 Tunnel and flow forcing

The final test was to install the turret inside the tunnel and measure its response to the combined forcing from the tunnel and aerodynamics. Similar to the analysis of tunnel-only forcing, we look first at the spectra of the modal response coefficient, q. The spectra of the first 5 modes are shown, along with the spectra from the case where the turret was outside the tunnel, in Fig. 20 for the M = 0.3 run. Similarly to tunnel-only forcing case and the hammer test, there is a distinct peak at the natural frequency for all modes, however, for the first 3 modes there is also a smaller peak at 765 Hz. Mode 1 only see a slight increase compared to the turret outside case, while mode 2 has a more significant increase in the range of 100 - 400 Hz. Mode 3 has increased energy over a much larger range of 100 - 800 Hz.

The modal forcing coefficient spectra for the first 3 modes are shown in Fig. 21 and look quite similar to the case for the turret outside the tunnel. Again we see good agreement between the forcing found using the theoretical and measured receptances in the neighborhood of the mode natural frequencies. The BIRMS, $\sigma_{f,\mathrm{BI}}$,

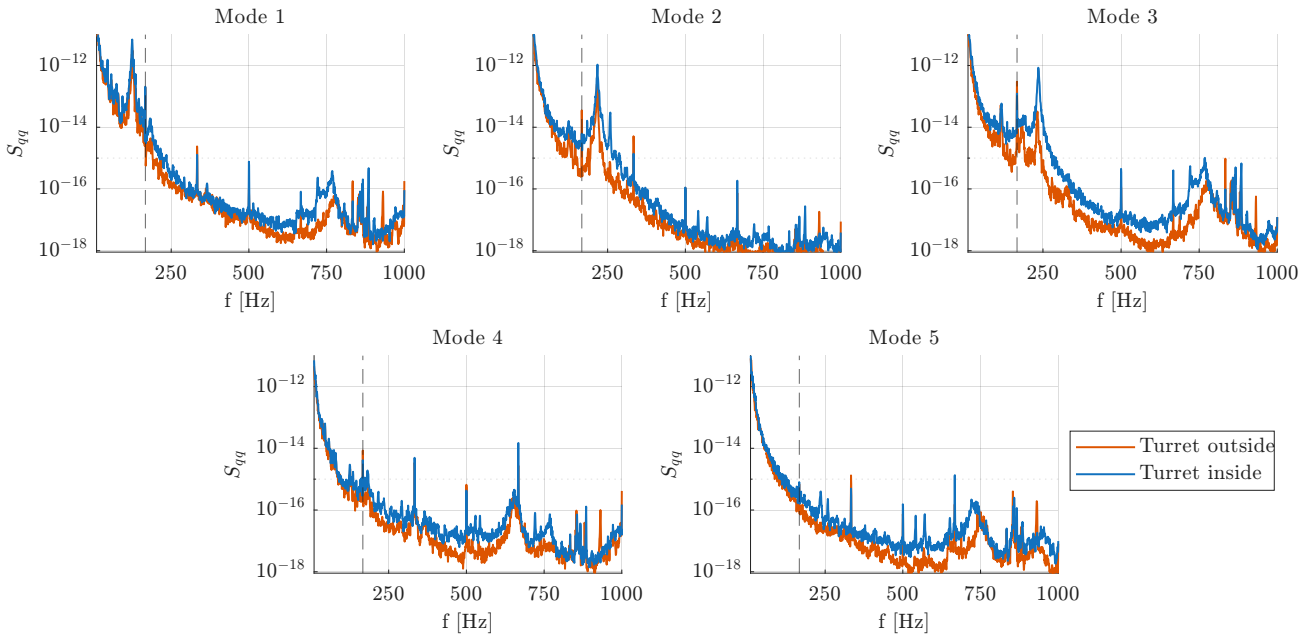

Figure 20. Modal response spectra for case where turret is inside tunnel.

was calculated for each run and is shown as a function of Mach number in Fig. 22. The forcing of all modes increases with Mach number and the relative magnitude of the forcing of each mode is similar, however, mode 2 has a significant increase compared to the case where the turret was outside the tunnel as it is exposed to significant spanwise aerodynamic forcing as was shown in Ref.[25]

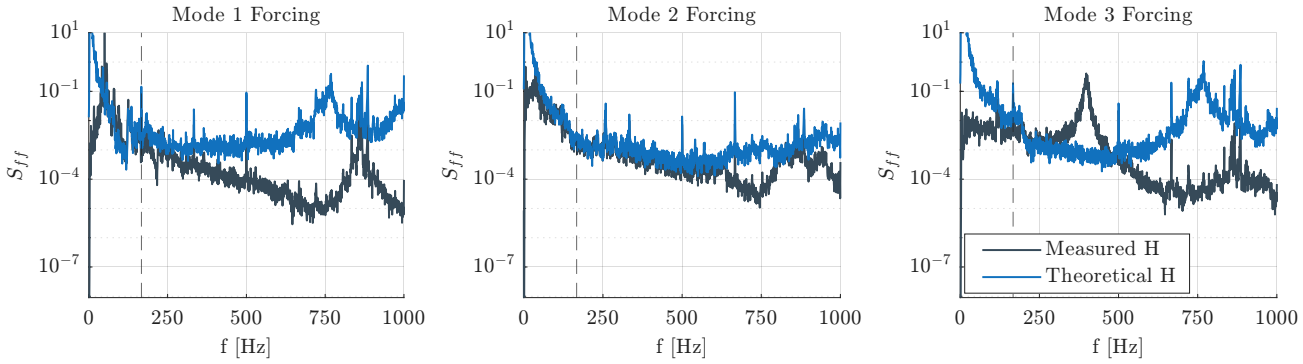

Figure 21. Modal forcing spectra computed using measured receptance and theoretical receptance for turret inside wind tunnel.

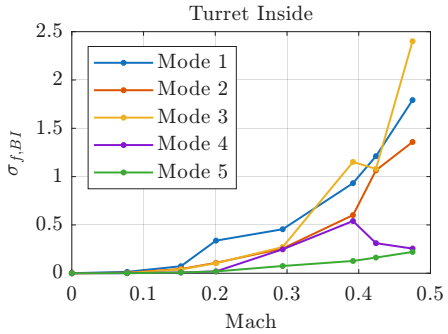

Figure 22. BIRMS modal forcing as a function of Mach number for turret inside tunnel.

Looking next at the jitter spectra we see similar spectral distributions for the SHWFS measurement and the jitter from the modal model, shown in Fig. 23; however, the modal model underestimates the jitter amplitude over the entire frequency range of interest. The BIRMS of jitter as a function of Mach number is presented in Fig. 24. Here we see the modal reconstruction underestimates jitter by about half across the Mach numbers tested. It is unclear why there is such significant underestimation and more analysis is required to explore this. In this test the air in the tires supporting the optical table were refilled and as a result the rms jitter energy in the range 50-100 Hz is not present.

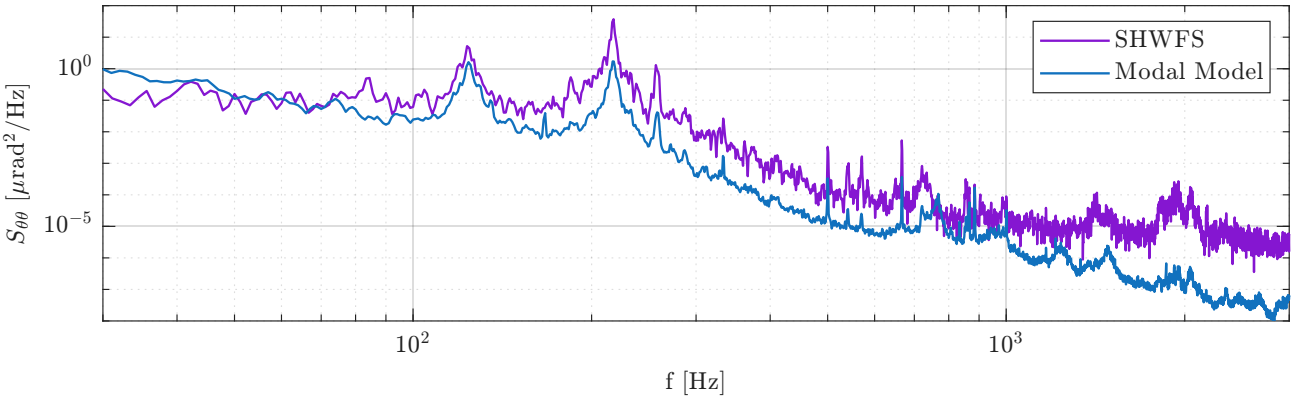

Figure 23. Jitter spectra for case where turret is mounted inside of wind tunnel.

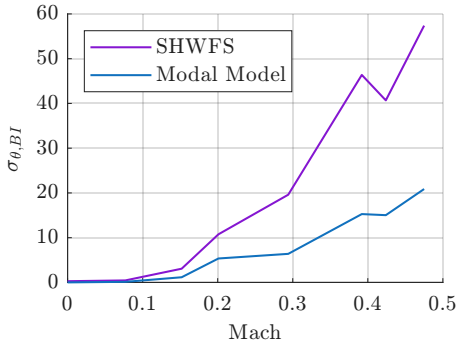

Figure 24. BIRMS jitter as a function of Mach number for turret inside.

Surface pressure measurements were also recorded to measure aerodynamic forcing. The pressure spectra are shown in Fig. 25 for Kulite 3, which is located on the side of the turret. Here it is plotted as a function of the non-dimension frequency Strouhal number, where $St_D = fD/U_\infty$ and D is the turret diameter, and U_∞ is the freestream velocity. It is well known that the frequency range around $St_D = 0.2$ is associated with spanwise anti-symmetric shedding from the hemispherical turret.[10,11,16] As the Mach number increases from 0.3 to 0.4 we see a dramatic increase in energy around $St_D = 0.2$. Additionally, starting at M = 0.4 we begin to see a strong narrowband peak at the wind tunnel blade passing frequency.

The Kulite pressure measurements were used to reconstruct the modal forcing coefficient from the pressure field via the LSE method described above. The spectra of the resulting coefficients are shown in Fig. 26 for the M=0.3 run. The dashed line shows $St_D = 0.2$. We can see there is a significant drop in forcing for frequencies above 200 Hz for all modes. Modes 1 and 3 have a slight broadband peak in energy around $St_D = 0.4$ which is the frequency range associated with symmetric shedding from the turret in a wake "breathing mode".[10,46]

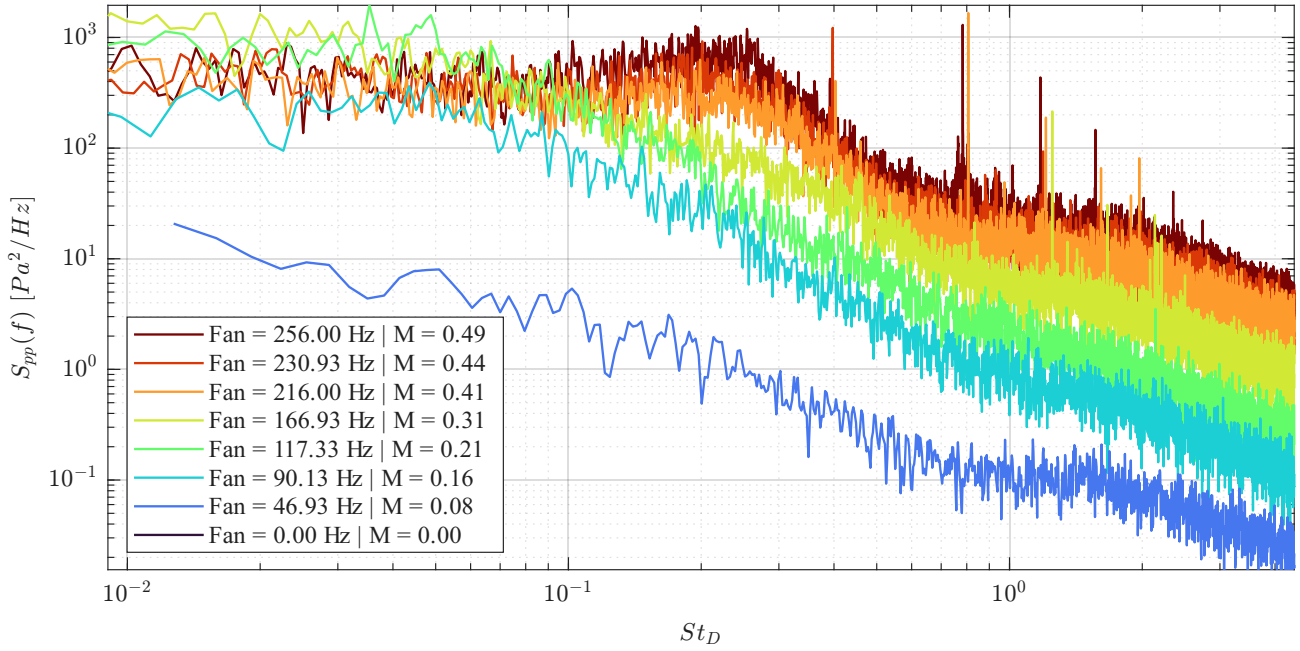

Figure 25. Pressure spectra for Kulite 3 on the side of the turret.

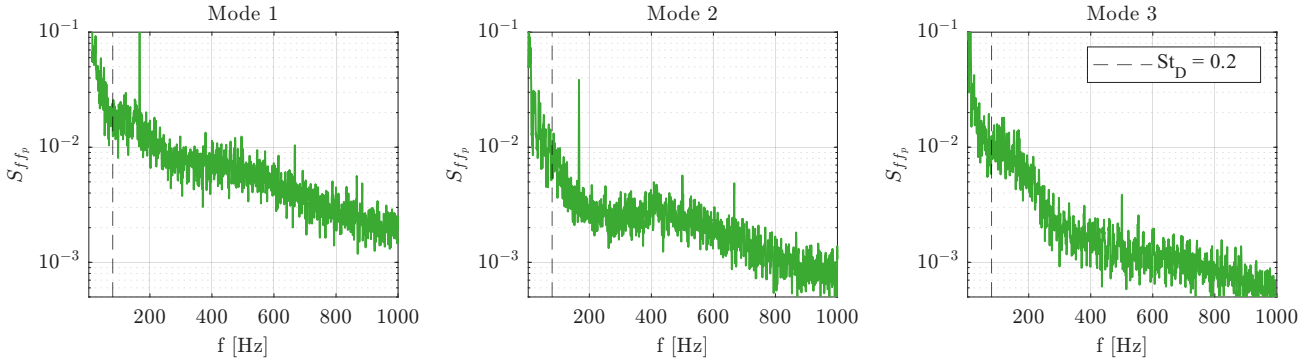

Figure 26. Modal forcing spectra computed from pressure measurement.

5. CONCLUSION

In this work, a modal model was developed to study the vibration of a hemispherical turret and the resulting beam jitter. A series of experiments were performed which involved a calibrated hammer test to characterize the modal model's accuracy, followed by wind tunnel testing with the turret mounted outside of the wind tunnel to isolate forcing from the tunnel vibration. Finally, wind tunnel testing was conducted with the turret mounted inside the wind tunnel, where it is exposed to the forcing of both the wind tunnel base vibration and the aerodynamic forcing. A sensor placement study was performed to find the optimal location of accelerometers and pressure sensors in order to accurately calculate modal response and forcing coefficients, respectively.

Calibrated hammer tests allow for the computation of the modal damping coefficient which was found to be approximately 1% for the first three vibrational modes and about 3% for modes 4 and 5. The modal receptance was compared with measured receptance and showed good agreement around the natural frequency ($\pm$25 Hz), but the first 3 modes showed a strong peak at the natural frequency of mode 5 which led to disagreement with the theoretical receptance over a wide range of frequencies. However, the frequency response functions showed good agreement with theory, suggesting that the mode 5 peak may be an non-physical artifact created when the accelerometer data were converted to the modal coordinates. The modal forcing was calculated and compared with the measured hammer force, but due to mode 5 contamination the modal coefficient data, the forcing is only accurate within about $\pm$25 Hz of the natural frequency.

For the case when the turret was mounted outside of the wind tunnel, the forcing of all modes was shown to increase with Mach number with modes 1 and 3 seeing the largest forcing, while modes 4 and 5 had the lowest. The jitter spectrum was also modeled using the modal-based model and was found to agree well for the peak on mode 1 but to underestimate mode 2, leading to an overall underestimate of rms jitter. Similar trends were found in the forcing for the case when the turret was mounted inside the tunnel, but the measured jitter had about double the magnitude of the model. In this case, the jitter estimate from the modal model underpredicted the jitter measurement over all frequencies of interest (between 100-1000 Hz). The forcing calculated using the pressure sensors had weak broadband peaks in modes 1 and 3 at $St_D \approx 0.4$, which is associated with the symmetric vortical shedding over the turret. However, no clear peaks were visible in the forcing at $St_D \approx 0.2$, which is associated with the anti-symmetric alternating vortex shedding over the sides of the turret. Further analysis is needed to investigate this unexpected result. The magnitude of the pressure forcing was between the forcing for the turret outside case and the turret inside case.

In the future, we will continue to study the forcing components and better quantify how the cases with the turret outside and inside the tunnel relate. There is clear influence from the wind tunnel fan blade pass frequency, so acoustic effects should be studied as well. The methodology used to compute the modal response coefficient from the accelerometer data also needs to be reviewed to understand why there is such a strong peak at the mode 5 natural frequency in the receptance for modes 1 - 3.

ACKNOWLEDGMENTS

The authors would like to thank Dr. Patrick Walgren and Dr. Andrew Oliva for discussion pertaining to this work. This work is supported by the Air Force Research Lab, Cooperative agreement number FA9451-23-2-0016. The U.S. Government is authorized to reproduce and distribute reprints for governmental purposes notwithstanding any copyright notation thereon. Auxiliary support was received from the Directed Energy Professional Society (DEPS) graduate research grant. Timothy Bukowski is supported by the National Defense Science and Engineering Graduate (NDSEG) Fellowship and by the Arthur J. Schmitt Presidential Leadership Fellowship.

DISCLOSURES

The views expressed are those of the author and do not necessarily reflect the official policy or position of the Department of the Air Force, the Department of Defense, or the U.S. Government. Distribution Statement A. Approved for public release; distribution is unlimited. Public Affairs release approval # AFRL-2025-3617.

REFERENCES

[1] Ross, C. L., "Origins of the airborne laser," *Air Power History* **58**(1) (2011).

[2] Kyrazis, D. T., "Airborne Laser Laboratory departure from Kirtland Air Force Base and a brief history of aero-optics," *Optical Engineering* **52**(7), 1 – 6 (2012).

[3] Jumper, E. J., Zenk, M. A., Gordeyev, S. V., Cavalieri, D. A., and Whitely, M., "Airborne Aero-Optics Laboratory," *Optical Engineering* **52**(7), 1 – 12 (2013).

[4] Gordeyev, S., Jumper, E. J., and Whiteley, M., [*Aero-Optical Effects: Physics, Analysis and Mitigation*], Wiley (2023).

[5] Kalensky, M., Gordeyev, S., Kemnetz, M., and Spencer, M., "Aero-optical effects, part I. System-level considerations: tutorial," preprint on Optica Open at https://preprints.opticaopen.org/articles/preprint/Aero-optical_effects_part_I_System-level_considerations_tutorial/26142928 (July 2024).

[6] De Lucca, N. G., Gordeyev, S., Jumper, E. J., Hird, K., Juliano, T. J., Gregory, J., Thordahl, J., and Wittich, D. J., "The estimation of the unsteady aerodynamic force applied to a turret in flight," in [*44th AIAA Plasmadynamics and Lasers Conference*], San Diego, CA, AIAA Paper 2013-3136 (June 2013).

[7] Gordeyev, S., De Lucca, N., Jumper, E., Hird, K., Juliano, T., Gregory, J., Thordahl, J., and Wittich, D., "Comparison of unsteady pressure fields on turrets with different surface features using pressure-sensitive paint," *Experiments in Fluids* **55**(1) (2014).

[8] De Lucca, N. G., Gordeyev, S., Morrida, J. J., and Jumper, E. J., "Investigation of flow dynamics over turrets with different spanwise aspect ratios using psp," in [*2018 AIAA Aerospace Sciences Meeting*], Kissimmee, FL, AIAA Paper 2018-2047 (January 2018).

[9] Gordeyev, S., De Lucca, N. G., Morrida, J. J., and Jumper, E. J., "Conditional studies of the wake dynamics of hemispherical turret using psp," in [*2018 AIAA Aerospace Sciences Meeting*], Kissimmee, FL, AIAA Paper 2018-2048 (January 2018).

[10] Bukowski, T. J., Gordeyev, S., Kalensky, M., and Kemnetz, M. R., "Study of unsteady surface flowfields on and around turrets with different protrusions," *AIAA Journal* **61**(12), 5320–5331 (2023).

[11] De Lucca, N. G., Gordeyev, S. V., and Jumper, E. J., "In-flight aero-optics of turrets," *Optical Engineering* **52**(7), 1 – 14 (2013).

[12] Morrida, J. J., De Lucca, N. G., Gordeyev, S., and Jumper, E. J., "Simultaneous pressure and optical measurements around a hemispherical in subsonic and transonic flight," in [*AIAA Flight Testing Conference*], Denver, CO, AIAA Paper 2017-3654 (June 2017).

[13] Morrida, J., Gordeyev, S., De Lucca, N., and Jumper, E. J., "Shock-related effects on aero-optical environment for hemisphere-on-cylinder turrets at transonic speeds," *Appl. Opt.* **56**, 4814–4824 (Jun 2017).

[14] Malkus, M. J., Frede, M. T., Sherer, S. E., and Garmann, D. J., "Effect of submergence on transonic flow around a hemisphere," *AIAA Journal* **60**(11), 1–15 (2022).

[15] Jelic, R., Sherer, S., and Greendyke, R., "Simulation of various turrets at subsonic and transonic flight conditions using overflow," *Journal of Aircraft* **50**(2), 398–409 (2013).

[16] Gordeyev, S. and Jumper, E., "Fluid dynamics and aero-optics of turrets," *Progress in Aerospace Sciences* **46**(8), 388–400 (2010).

[17] Kalensky, M., *Airborne Measurement of Atmospheric-Induced Beam Jitter*, PhD thesis, University of Notre Dame (2022).

[18] Kemnetz, M. R., *Analysis of the Aero-Optical Component of the Jitter Using the Stitching Method*, PhD thesis, University of Notre Dame (2019).

[19] De Lucca, N., *Studies of the pressure field and related beam jitter for hemisphere-on-cylinder turrets*, PhD thesis, University of Notre Dame (2016).

[20] De Lucca, N. G., Gordeyev, S., and Jumper, E., "The study of aero-optical and mechanical jitter for flat window turrets," in [*50th AIAA Aerospace Sciences Meeting including the New Horizons Forum and Aerospace Exposition*], Nashville, TN, AIAA Paper 2012-0623 (January 2012).

[21] De Lucca, N. G., Gordeyev, S., and Jumper, E. J., "Effect of surface unsteady pressure field on global beam jitter for a hemisphere-on-cylinder turret," in [*52nd Aerospace Sciences Meeting*], National Harbor, MD, AIAA Paper 2014-0322 (January 2014).

[22] Merritt, P. and Sher, L., "Summary of aerodynamic vibration effects on an airborne turret," in [*Aero-Optical Phenomena*], Gilbert, K. G. and Otten, L. J., eds., **80**, 343–356, American Institute of Aeronautics and Astronautics (January 1982).
[23] Griffin, S. F. and Kelchner, B. L., "Line-of-sight jitter for advanced tactical laser," *AIAA Journal* **61**(7), 3204–3209 (2023).
[24] Merritt, P. and Spencer, M., [*Beam Control for Laser Systems*], ch. 3. System Engineering, Performance Equations, and Error Budgets, 84–87, The Directed Energy Professional Society (2018).
[25] Roeder, A. L. and Gordeyev, S., "Wake response downstream of a spanwise-oscillating hemispherical turret," *Journal of Fluids and Structures* **109**, 103470 (2022).
[26] Kalensky, M., Catron, B., Gordeyev, S. V., Jumper, E. J., and Kemnetz, M., "Investigation of aero-mechanical jitter on a hemispherical turret," in [*Proceedings of SPIE*], Dolne, J. J. and Spencer, M. F., eds., SPIE (August 2021).
[27] Griffin, S., Blackburn, J., Wittich, J., Gordeyev, S., and Jumper, E. J., "Integrated line-of-sight modeling of the airborne aero-optics laboratory," in [*Proceedings of the Advanced Maui Optical and Space Surveillance Technologies Conference*], Ryan, S., ed. (September 2013).
[28] Bukowski, T. J., Rennie, R. M., Gordeyev, S., and Kemnetz, M., "Preliminary aero-mechanical jitter analysis of hemispherical turrets," in [*Unconventional Imaging, Sensing, and Adaptive Optics 2024*], Dolne, J. J., Bose-Pillai, S. R., and Kalensky, M., eds., **13149**, 131490E, International Society for Optics and Photonics, SPIE (2024).
[29] Lucca, N. G. D., Catron, B. L., and Kemnetz, M. R., "Analytical jitter scaling relationships for airborne optical applications," in [*Unconventional Imaging, Sensing, and Adaptive Optics 2024*], Dolne, J. J., Bose-Pillai, S. R., and Kalensky, M., eds., **PC13149**, PC1314906, International Society for Optics and Photonics, SPIE (2024).
[30] He, J. and Fu, Z.-F., [*Modal Analysis*], Butterworth-Heinemann, Woburn, MA (2001).
[31] Ewins, D. J., [*Modal Testing: Theory and Practice*], Research Studies Press u.a. (1984).
[32] Dossing, O., "Structural testing part 1: Mechanical mobility measurements (bruel and kjaer)." https://pearl-hifi.com/06_Lit_Archive/15_Mfrs_Publications/10_Bruel_Kjaer/07_Primers_and_Handbooks/Structural_Testing_Pts_1-2.pdf (1988). Accessed: 2025-01-18.
[33] Dossing, O., "Structural testing part 2: Modal analysis and simulation (bruel and kjaer)." https://pearl-hifi.com/06_Lit_Archive/15_Mfrs_Publications/10_Bruel_Kjaer/07_Primers_and_Handbooks/Structural_Testing_Pts_1-2.pdf (1988). Accessed: 2025-01-18.
[34] Omar, S., "Experimental modal analysis for aerial centerline fuel tanks," *Algerian Journal of Research and Technology* **8**, 57–71 (May 2025).
[35] Harris, C. M., Piersol, A. G., and Paez, T. L., [*Harris' shock and vibration handbook*], McGraw-Hill Professional, New York, NY, 6 ed. (Nov. 2009).
[36] Hernley, V. L., *Identification of Aerodynamic Forcing Mechanisms from Experimental Measurements of Compressor Blade Vibration*, PhD thesis, University of Notre Dame (7 2023).
[37] Kim, W., Hwang, J.-S., Kwon, D.-K., and Kareem, A., "Cumulative power spectral density-based damping estimation," *Earthquake Engineering & Structural Dynamics* **53**(5), 1787–1802 (2024).
[38] Sandia National Laboratories, "sdynpy: Structural dynamics in python," (2024). GitHub repository.
[39] SDyPy Developers, "Sdypy: Structural dynamics python library," (2024). GitHub repository.
[40] MathWorks, *System Identification Toolbox User's Guide* (2024). Accessed: 2024-02-05.
[41] Bukowski, T. J., Rennie, M. R., and Gordeyev, S., "Sparse sensing and surface pressure field reconstruction for flow over a hemisphere," in [*AIAA SCITECH 2025 Forum*], American Institute of Aeronautics and Astronautics (Jan. 2025).
[42] Adrian, R. J., "On the role of conditional averages in turbulence theory," in [*Turbulence in Liquids: Proceedings of the 4th Biennial Symposium on Turbulence in Liquids*], Patteson, G. and Zakin, J., eds., 323–332, Science Press, Princeton (1977).
[43] Williams, J. P., Zahn, O., and Kutz, J. N., "Sensing with shallow recurrent decoder networks," (2023).

[44] Drmač, Z. and Gugercin, S., "A new selection operator for the discrete empirical interpolation method—improved a priori error bound and extensions," *SIAM Journal on Scientific Computing* **38**(2), A631–A648 (2016).

[45] Manohar, K., Brunton, B. W., Kutz, J. N., and Brunton, S. L., "Data-driven sparse sensor placement for reconstruction: Demonstrating the benefits of exploiting known patterns," *IEEE Control Systems Magazine* **38**(3), 63–86 (2018).

[46] De Lucca, N. G., Gordeyev, S., Morrida, J. J., Jumper, E. J., and Wittich, D. J., "Modal analysis of the surface pressure field around a hemispherical turret using pressure sensitive paint," in [*2018 AIAA Aerospace Sciences Meeting*], Kissimmee, FL, AIAA Paper 2018-0932 (January 2018).